

## Variability in iron (II) oxidation kinetics across diverse hydrothermal sites on the northern Mid Atlantic Ridge

González-Santana David <sup>1,\*</sup>, González-Dávila Melchor <sup>2</sup>, Lohan Maeve C. <sup>3</sup>, Artigue Lise <sup>4</sup>, Planquette Helene <sup>1</sup>, Sarthou Geraldine <sup>1</sup>, Tagliabue Alessandro <sup>5</sup>, Santana-Casiano J. Magdalena <sup>2</sup>

<sup>1</sup> Univ Brest, CNRS, IRD, Ifremer, LEMAR, F-29280 Plouzane, France

<sup>2</sup> Instituto de Oceanografía y Cambio Global, IOCAG, Universidad de Las Palmas de Gran Canaria, Las Palmas de Gran Canaria, Spain

<sup>3</sup> Ocean and Earth Science, University of Southampton, National Oceanography Centre, Southampton SO14 3ZH, United Kingdom

<sup>4</sup> LEGOS, University of Toulouse, CNRS, CNES, IRD, UPS, 31400 Toulouse, France

<sup>5</sup> School of Environmental Sciences, University of Liverpool, Liverpool, United Kingdom

\* Corresponding author : David González-Santana, email address : [david.gonzalezsantana@univ-brest.fr](mailto:david.gonzalezsantana@univ-brest.fr)

### Abstract :

One of the recently recognized main sources of iron to the deep ocean inventory is the hydrothermal activity associated with mid-ocean ridges. Little is known about the oxidation kinetics of iron(II) within these environments, especially the dependence on physico-chemical parameters such as temperature (T), pH, particle size-fractionation and the effect of organic matter.

Following sample collection during the GA13 section cruise, the iron(II) oxidation at six hydrothermal vent sites (Menez Gwen, Lucky Strike, Rainbow, Lost City, Broken Spur and TAG) along the Mid-Atlantic Ridge were investigated, revealing high variability. The Fe(II) oxidation rate constant analysis from multiple stations at two sites (Rainbow and TAG), revealed that factors, other than T and pH, controlled the oxidation process. Experiments on the effect of particle size-fractionation and organic matter at different pH showed that the presence of organic ligands and colloidal size particles delayed the oxidation process, while not affecting the overall pH dependency.

Extending our analysis to the broader relationship between the Fe(II) oxidation rate constants across a range of temperatures (between 2 and 25 °C) and pH (between 7 and 8) on a set of selected hydrothermal samples allowed us to derive a multiparametric equation to model the iron(II) oxidation rate constants in the ocean. This equation covers a larger range of temperatures than previous published equations, improving its applicability for global biogeochemical models.

---

## Highlights

► Organic ligands and nanoparticles increase the resistance to oxidation. ► We present an improved multiparametric equation to calculate Fe(II) oxidation rates. ► Oxidation rates close to the vent sites are systematically faster than theorized.

**Keywords** : Fe(II) oxidation kinetics, Fe(II) half-life time, Kinetic equation, Hydrothermal, Mid Atlantic Ridge

## 38    **1 Introduction**

39    It is now well-established that phytoplankton growth is limited by the concentration of  
40    dissolved iron (Fe) in up to 30% of the world oceans (Moore et al., 2013). Iron in the ocean,  
41    can be found as both ferric (Fe(III)) and ferrous (Fe(II)) iron, where 99% of the dissolved  
42    Fe(III) is complexed by organic ligands (Rue and Bruland, 1995). In oxic waters, Fe(II) tends  
43    to oxidize to the most thermodynamically stable form, Fe(III), in a period of minutes to hours

(Santana-Casiano et al., 2005). Oxidation of Fe causes the solubility to decrease (Millero et al., 1995), therefore, reducing its bioavailability (Shaked et al., 2005; Morel et al., 2008).

Recently, in the context of the international GEOTRACES program ([www.geotraces.org](http://www.geotraces.org)), several studies showed that Fe supplied by hydrothermal activity from mid-ocean ridges can have a substantial impact on Fe distributions at basin scales (Tagliabue et al., 2010; Conway and John, 2014; Resing et al., 2015; Fitzsimmons et al., 2017; Tagliabue et al., 2017).

Hydrothermal vent supply of dFe is required to reproduce deep ocean observations (Tagliabue et al., 2010) could represent up to 11-22 % of the dissolved iron (dFe, filtered by 0.2  $\mu\text{m}$ ) present in the deep ocean globally (Bennett et al., 2008), accounting for a similar dFe flux as continental riverine runoff (Elderfield and Schultz, 1996). Therefore, hydrothermalism acts as an important Fe source in the deep ocean which may affect the global biological carbon pump (Tagliabue et al., 2010; Resing et al., 2015).

The concentration of dissolved Fe(II) (dFe(II)) in the open ocean is very low, between 0.02 and 2  $\text{nmol L}^{-1}$ , due to its fast oxidation under oxic conditions following the Fenton reaction mechanism (González-Davila et al., 2005; Santana-Casiano et al., 2005). However, specific oceanic regions present dFe(II) concentrations which are orders of magnitude higher. In marine sediment interstitial waters, concentrations can reach around 300  $\mu\text{mol L}^{-1}$  (de Baar and De Jong, 2001), upwelling systems can increase Fe(II) concentrations up to 50  $\text{nmol L}^{-1}$  (Hong and Kester, 1986), while hydrothermal fluids can contain as much as 25  $\text{mmol L}^{-1}$  of dFe(II) (German and Von Damm, 2004). Water emanating from hydrothermal systems contains high concentrations of Fe(II) amongst other elements (Mottl et al., 1979; Mandernack and Tebo, 1993). Studies conducted at hydrothermal vent sites in different ocean basins have revealed different Fe(II) oxidation rate constants, with Fe(II) half-life times varying from 0.5 to 220 min, which has important implications for the dispersion of produced

68 Fe-oxide phases (Massoth et al., 1998; Field and Sherrell, 2000; Statham et al., 2005; Wang  
69 et al., 2012; Santana-González et al., 2017; Rouxel et al., 2018). Recently, Gartman and  
70 Findlay (2020) compiled all the available data for Fe(II) half-life from four hydrothermal  
71 systems. One site was the TAG vent site in the Atlantic Ocean, while the others were located  
72 in the Indian and Pacific Oceans, with Fe(II) half-life estimated using large Fe(II) spikes (500  
73 nmol L<sup>-1</sup>) that may affect the role played by different reactive oxygen species (González-  
74 Dávila et al., 2006).

75 Temperature (T), pH, and oxygen concentration (O<sub>2</sub>) are the primary variables known to  
76 directly affect the Fe(II) oxidation (Stumm and Lee, 1961; Millero et al., 1987; Millero and  
77 Sotolongo, 1989; Santana-Casiano et al., 2005). Salinity also affects the Fe(II) oxidation, as  
78 reported in previous laboratory experiments (Millero et al., 1987; Santana-Casiano et al.,  
79 2005). However, other factors such as changes in the inorganic complexation of Fe(II) due to  
80 the specific ionic composition of the vent fluid, or organic complexation can influence these  
81 oxidation rate constants (Rose and Waite, 2003; Statham et al., 2005). Therefore, the  
82 oxidation rate constants must be termed “apparent” due to the effect of organic complexation  
83 (Voelker and Sulzberger, 1996), as the nature and concentrations of organic ligands vary  
84 between samples. Moreover, pyrite nanoparticles formed in hydrothermal vent sites, have  
85 been estimated to oxidize more slowly than dissolved Fe(II) (Yücel et al., 2011), showing  
86 that particle composition also influences the oxidation rate constants. The first empirical  
87 equation describing the Fe(II) oxidation rate constants in seawater was reported by Millero et  
88 al. (1987), and later updated by Santana-Casiano et al. (2005) for nanomolar concentrations.  
89 This equation has been included in coupled physical-biogeochemical models in the ocean  
90 (OGCBMs) to explore the impact of future climate change on the oxidation of Fe(II)  
91 (Tagliabue and Völker, 2011). However, this equation was established for water temperatures

ranging from 10 to 25 °C, which leads to discrepancies for the Fe(II) oxidation rate constants for cold, deep ocean water masses.

The aims of this study were to measure the oxidation kinetic constants ( $k'$ ) of Fe(II) from different hydrothermal vents and to investigate whether the variations of pH, T and S can explain the observed variability, or if other factors such as the presence of particles, colloids or dissolved organic matter (DOM) are significant contributors. This updated version of the equation incorporates a wider range of temperatures, which lowers the error associated with the theoretical Fe(II) oxidation rate constants. Thus, it becomes applicable to the calculation of theoretical Fe(II) oxidation for the deep waters in which hydrothermal systems are typically found.

## 2 Methods

### 2.1 Sampling sites and characteristics

Seawater samples were collected during the GA13 section cruise (JC156) along the Mid Atlantic Ridge (MAR) onboard the *RRS James Cook*. This cruise departed Southampton, UK on December 20<sup>th</sup>, 2017 and arrived into Guadeloupe, France on February 1<sup>st</sup>, 2018.

Alongside the large scale ocean section survey, sampling focused on six hydrothermal vent sites along the MAR: Menez Gwen (37° 50'N 31° 31'W; Charlou et al., 2000), Lucky Strike (37° 17'N 32° 16'W; Charlou et al., 2000), Rainbow (36° 14'N 33° 54'W; Douville et al., 2002), Lost City (30° 7'N 42° 7'W; Kelley et al., 2001), Broken Spur (29 °N; James et al., 1995), and TAG (26°N; Gamo et al., 1996) (Fig. 1). These six hydrothermal vent sites represent a wide range of possible hydrothermal conditions due to different underlying geological conditions. Lost City and Menez Gwen are the shallowest sites, with the vent site depths located at 700-720 m and 840-850 m, respectively. The Lucky Strike hydrothermal

115 field is situated between 1560 and 1730 m depth. The Rainbow vent site is found at 2270-  
116 2280 m, within the average range (2000-3000 m) of oceanic ridge depth (Searle, 2013), while  
117 Broken Spur and TAG are deeper hydrothermal systems located at 3100-3300 m and 3670-  
118 3700 m, respectively. Chemically, Lost City is an alkaline hydrothermal vent, with pH  
119 ranging from 9.0 to 9.8. The vent fluid is at a lower temperature of 40-75 °C, compared to  
120 185-365 °C at the other vent sites and has extremely low concentrations of most trace  
121 elements (e.g. Fe below the detection limit compared to 2-24000  $\mu\text{mol L}^{-1}$  at the other vent  
122 sites) (Ludwig et al., 2006; Fouquet et al., 2013). All other hydrothermal vent sites are acidic  
123 with pH lower than 4, and act as important sources of trace metals (Charlou et al., 2000;  
124 Douville et al., 2002; Andreani et al., 2014). Geologically, Menez Gwen and Lucky Strike are  
125 similar, their basement rocks are mafic, enriched-Mid-Ocean Ridge Basalt (E-MORB,  
126 enriched with light rare earth elements, LREE), and present sulfide mounds. Rainbow also  
127 presents sulfide mounds, but its basement rock is ultramafic. Further south, the alkaline Lost  
128 City is also situated above an ultramafic base with carbonate chimneys. Finally, Broken Spur  
129 and TAG have sulfide mounds and basement rocks formed by normal-MORB (N-MORB,  
130 LREE depletion) (references within Fouquet et al., 2010).

131 Seawater samples were collected according to the GEOTRACES guidelines  
132 (<http://www.geotraces.org/images/Cookbook.pdf>). Briefly, a titanium rosette fitted with 24 x  
133 10 L trace metal-clean Teflon-coated OTE (Ocean Test Equipment) bottles, a CTD profiler  
134 (Sea-bird Scientific), light scattering sensor (PMEL MAPR), and a redox potential sensor  
135 (PMEL MAPR), were deployed on a conducting Kevlar wire to collect samples from the  
136 water column. Sampling depths were actively chosen from the continuous T, salinity (S),  
137 light scattering sensor ([https://data-](https://data-search.nerc.ac.uk:443/geonetwork/srv/api/records/8ba648f2759d57fbb2246671f8065939)  
138 [search.nerc.ac.uk:443/geonetwork/srv/api/records/8ba648f2759d57fbb2246671f8065939](https://data-search.nerc.ac.uk:443/geonetwork/srv/api/records/8ba648f2759d57fbb2246671f8065939))  
139 and redox potential readings.

Upon recovery, the OTE bottles were transported into an ISO class 6 clean air van. Unfiltered samples (UF) for Fe(II) oxidation kinetics were immediately transferred into thoroughly rinsed acid-cleaned 250 mL or 1 L low-density polyethylene bottles (LDPE; Nalgene) following the GEOTRACES Cookbook (<http://www.geotraces.org/images/Cookbook.pdf>) and frozen at -20 °C. Samples remained frozen in a -20 °C freezer for one year before their analysis. pH samples were collected in 125 mL borosilicate bottles and kept in the dark until the time of analysis.

## **2.2 pH determination**

pH was measured onboard and during laboratory-based kinetic experiments in the free scale using a Tris buffer solution (Millero, 1986). Onboard pH samples were kept in the dark, inserted into a 25 °C water bath, and measured at 25 °C, within less than 1 hour after collection. Laboratory-based kinetic experiments used a Titrino 719 (Metrohm™) which automatically added 0.01M hydrochloric acid (HCl, PANREAC Hiperpur-plus) in order to keep the pH constant. The pH at *in situ* conditions were computed considering the total alkalinity for an average profile of the area (Key et al., 2015; Olsen et al., 2016). The average profile was obtained from plotting all the available alkalinity data from the studied region (20-30 °N and 40-50 °W). The associated error of the estimate was  $\pm 6 \mu\text{mol kg}^{-1}$ . Gray et al. (2011) showed that computed pH values are relatively insensitive to errors in alkalinity, and that pH measurements can be used to compute the magnitude and variability of inorganic carbon variables. A fluctuation of  $400 \mu\text{mol kg}^{-1}$  in total alkalinity values (e.g. from 2325 to  $2725 \mu\text{mol kg}^{-1}$ ) will change the pH in +0.005, which lies within the error of determination for potentiometric pH. The set of constants from Lueker et al. (2000) were used.

All the pH data in the text and in the figures, including kinetics and profile data are expressed in the free scale.



### 2.3 Fe(II) measurements

In order to measure the Fe(II) oxidation rate constants, continuous Fe(II) concentrations were determined using the FeLume System (Waterville Analytical), with a data point acquisition every 1 s. This direct Flow Injection Analysis system uses luminol (5-amino-2,3-dihydro-1,4-phthalazinedione, Sigma-Aldrich) as the reagent (King et al., 1995) which reacts with Fe(II). The sample was continuously aerated with pure air (Carbueros Metalicos S.A.). A 0.8 nmol L<sup>-1</sup> addition of Fe(II) (ammonium iron(II) sulfate hexahydrate, Sigma-Aldrich) was introduced into each sample and the Fe(II) concentration was continuously monitored until the signal had reduced by 70 %. This method produces apparent rate constants ( $k_{app}$ ) because the oxidation rate constant is measured on a Fe(II) spike rather than on the ambient Fe(II). Although, the oxidation rate constant is not affected by the initial Fe(II) in solution (Millero et al., 1987; Roy et al., 2008; Roy and Wells, 2011; Santana-González et al., 2018), the equilibrium with the organic ligands and particle surfaces could be affected. Moreover, due to the effects of organic complexation and that the concentrations of the organic ligands in each sample are not constant, the apparent oxidation rate constants are consequently not true constants.

Some previous oxidation kinetic studies have found a second-order dependency of the Fe(II) concentration against time (e.g. Statham et al., 2005). However, in oxygen saturated samples a pseudo-first order rate dependency was obtained, where the slope ( $\ln([\text{Fe(II)}])$  against time) represents the pseudo-first order rate constant  $k'$  (Eq. 1). The linearity remained longer than the half-life time and was thus considered acceptable in all the analyses ( $R^2 = 0.983 \pm 0.017$ ,  $n \text{ samples} = 298$ ). The observed linearity confirms that the equilibrium between the added Fe(II) with organic ligands and particles is achieved before 30 s (our first Fe(II) determination time limit). The  $k'$  error associated with these high  $R^2$  values was 2% for *in*

188 *situ* condition experiments, and 1% for experiments carried out at 25 °C. The half-life ( $t_{1/2}$ ) of  
 189 Fe(II) in seawater can be calculated from  $k'$  (Eq. 1 and 2).

$$190 \quad d[Fe(II)]/dt = -k_{app}[O_2][Fe(II)] \quad (1)$$

191 In oxygen saturated concentrations, the corresponding pseudo-first order rate constant  $k' =$   
 192  $k_{app}[O_2]$ .

$$193 \quad t_{1/2} = \ln(2)/k' \quad (2)$$

194 The minimum energy required to start the oxidation reaction (activation energy,  $E_a$ , J mol<sup>-1</sup>)  
 195 and the corresponding preexponential or frequency factor (A) were computed from the  
 196 calculated  $k'$  using the empirical Arrhenius equation, where R is the universal gas constant  
 197 (8.314 J mol<sup>-1</sup> K<sup>-1</sup>):

$$198 \quad \log(k') = \log(A) - \frac{E_a}{R \cdot \ln(10) \cdot T} \quad (3)$$

199 Iron (II) blanks were obtained from a 2 h aerated, magnetically stirred sample which was kept  
 200 in the dark to achieve the oxidation of Fe(II) (Santana-Casiano et al., 2005). Iron (II) in these  
 201 blanks always below the detection limit. Calibration curves (0 to 1 nmol L<sup>-1</sup>) were produced  
 202 daily and confirmed linearity in the Fe(II) signal. The detection limit, defined as three times  
 203 the standard deviation of the blank after being aerated for 10 minutes, was lower than 50  
 204 pmol L<sup>-1</sup>. Reproducibility was checked by running the same sample three times throughout  
 205 the day after an addition of 1 nmol L<sup>-1</sup> of Fe(II) with an agreement in concentrations that was  
 206 better than  $\pm 0.1$  nmol L<sup>-1</sup>. Accuracy could not be determined since reference materials  
 207 currently do not exist. Results are systematically given as  $t_{1/2}$  (in min), followed by the  
 208 measured  $k'$  (in min<sup>-1</sup>).

## 209 **2.4 Experimental setup**

Using natural seawater samples, kinetic experiments were carried out under different conditions, with pH and T set to *in situ* conditions (data shown in the supplementary Table S1), and with pH and T normalized to constant values, in unfiltered, filtered and filtered and UV-irradiated samples. These later experiments required a high sample volume, limiting the number of experiments.

The steps required for the Fe(II) oxidation kinetics determination are as follows. The day before the experiments, three to four frozen samples were taken out of the freezer and placed in a fridge set to 4 °C. The next morning, a temperature-controlled water bath was set to the coldest *in situ* potential temperature (supplementary Table S1). While the water bath was cooling down, each sample was subsampled into three 60 mL acid cleaned LDPE bottles and placed back into the fridge. One of the subsamples was inserted into the temperature-controlled water bath, which was set to the original *in situ* potential temperature of the sample. The sample was left in the water bath for acclimatization during 15 min and then transferred into the reaction vessel. In the reaction vessel, the sample was aerated prior to and during the study. After 10 minutes of aeration, the Fe(II) addition was made and the Fe(II) concentration and time were continuously monitored. After finishing with the coldest subsample, the temperature of the water bath was increased to the following coldest temperature, and the next sample was left to acclimate.

#### ***2.4.1 Quantification of the temperature and pH effect on the iron (II) oxidation rate constant***

In order to improve the temperature range of the existing Fe(II) oxidation kinetic equation, 1 L samples of deep ocean water were collected during the JC156 cruise, at stations 13 (2339 m), 16 (2051 m), 24 (2829 m), 30 (2700 m), 31 (2796 m), and 35 (1999, 3350 and 3601 m). The samples remained frozen at -20 °C during one year until analysis. Two days prior to the

analysis, samples were thawed in a 4 °C fridge. This allowed a slow melting of the samples in the dark, thus limiting any photoproduction of Fe(II) and also removal of any superoxide and hydroxyl radicals in the sample (Voelker and Sedlak, 1995).

The samples were then transferred into 60 mL LDPE bottles (one for each condition).

Temperature effect experiments were performed at constant pH, and those for pH effect at constant temperature. The temperature effect experiments were carried out at *in situ* temperature, 10, 20 and 25 °C at a fixed pH of 8. The pH effect experiments were carried out at *in situ* pH, and pH 7, 7.5 and 8 at a fixed temperature of 25 °C.

#### ***2.4.2 Oxidation rate constants through the water column at the six hydrothermal vent sites***

To assess the expected Fe(II) oxidation rate constants at *in situ* conditions, the experiments were carried out at *in situ* potential temperature and pH ( $T_{is}pH_{is}$ ). The temperature was then increased to 25 °C ( $T_{25}pH_{is}$ ) to obtain the temperature effect on the oxidation rate constants. A third set of experiments were performed at 25 °C and pH 8 ( $T_{25}pH_8$ ). The T and pH normalization of all the samples allowed for the interpretation of the effect of other variables, such as organic matter and particles, in the oxidation rate constants. This allows to investigate where seawater composition is influencing the oxidation rate, a process that cannot be isolated when comparing two samples with different temperatures and/or pH.

#### ***2.4.3 Experimental setup to assess the effect of colloidal and organic matter***

The unused unfiltered (UF) sample volumes remaining from the quantification of the temperature and pH effect experiments were used to assess the impact of particles, colloids and organic matter. Unfiltered samples underwent sequential filtration. Three aliquots were filtered through 0.2 µm (F0.2; Whatman® Anodisc), and one of them was then filtered through 0.02 µm (F0.02; Whatman® Anotop®), while the last aliquot was filtered through

0.02  $\mu\text{m}$  followed by UV-irradiation (F0.02+UV). All samples were left in the dark for 6 days to limit the effect of any photochemically generated reactive oxygen species (ROS) produced during the UV-irradiation (Yuan and Shiller, 2001; Roy et al., 2008). All samples were analyzed following the same procedure as for the assessment of the pH effect (see section 2.4.2 above). In order to assess whether the generated ROS species could affect the Fe(II) oxidation rate constants determined after 0.02  $\mu\text{m}$  filtration and UV-irradiation, the effect of the amount of hydrogen peroxide ( $\text{H}_2\text{O}_2$ ) generated during this process was considered (Yuan and Shiller, 2001; O'Sullivan et al., 2005). Other short-lived ROS species such as hydroxyl radicals were not accounted for, since their nanosecond half-life times do not allow for their determination using our analytical method.

## 3 Results

### *3.1 Temperature and pH effects on the oxidation rate constants*

Experiments for the temperature effect study were carried out at a pH of 8. When plotting  $\log k'$  vs.  $1/T$  ( $\text{K}^{-1}$ ) (Fig. 2, Eq. 3), results showed an average slope ( $-\Delta E_a/R/\ln(10)$ ) of  $-4992 \pm 232$ . Notably, the data obtained from samples collected west of TAG at 2700 m depth (Station 30) showed a slope of  $-3732 \pm 216$ , which is more than three standard deviations away from the average value. This lower slope corresponds to a much lower activation energy for this sample, with a value of  $71 \pm 4 \text{ KJ mol}^{-1}$ . This effect was probably caused by the interaction of organic compounds or particles with the Fe(II) species which affected the limiting Fe(II) oxidation step, and therefore a result of a different oxidation reaction mechanism. If this sample is removed, the average slope increases to  $-5434 \pm 183$ , and the activation energy of all the samples considered was  $104 \pm 3 \text{ KJ mol}^{-1}$ . These values are within the experimental error of previous determinations from Gulf Stream water ( $-5362 \pm 162$ , and an activation energy of  $103 \pm 3 \text{ KJ mol}^{-1}$ ; Santana-Casiano et al., 2005).

When experiments were carried out at a constant T of 25 °C and at 5 different pH values in the range from 7 to 8,  $\log k'$  and pH were linearly related, with slopes of  $1.00 \pm 0.06$  (Fig. 3) and with no data points outside of 3 standard deviations. As with the temperature relationship, the sample from the station West of TAG at 2700 m presented a slope ( $1.19 \pm 0.08$ ) out of the 1:1 dependence. A second sample, (TAG at 1999 m depth, over 1600 m above the vent site) showed a lower slope ( $0.81 \pm 0.12$ ).

The unique use of lower temperature samples in this study, allowed a better estimation of Fe(II) oxidation kinetic rate constants at temperatures lower than 10 °C, increasing the range of applicability of the Fe(II) oxidation kinetic equation of Santana-Casiano et al. (2005). Using the equation and dataset from Santana-Casiano et al. (2005), which had a wider range in pH and salinity, together with the additional pH data and a wider range of temperature from the present study, a revised equation was obtained. The pH and salinity dependence did not change, while the T relationship was modified (Eq. 4). Thus, an updated equation for the theoretical Fe(II) oxidation appropriate for deep waters is presented:

$$\log k' (s^{-1}) = 35.627 - 6.7109 * pH + 0.5342 * pH^2 - 5434.02/T - 0.04406 * S^{1/2} - 0.002847 * S \quad (4)$$

The T factor has been modified from  $-5362.6/T$  to  $-5434.02/T$  obtained from the average slope of Figure 2. To assess the performance of the updated Fe(II) oxidation kinetic equation (Eq. 4), it was compared to three existing equations. The chosen equations were the first derived equation (Millero et al., 1987), the equation by Santana-Casiano et al. (2005), and a recent equation using Labrador Seawater (Santana-González et al., 2019). The four equations were compared to the measured oxidation rate constants at *in situ* pH and T conditions. The residual sum of squares (RSS) and root mean square error (RMSE) between predicted and observed values were calculated. Smallest values of RSS and RMSE indicate the best

equation fit to observations. Additionally, the difference in logarithms of the likelihood ( $\Delta\log(L)$ ), based on a Gaussian error distribution with a constant variance of log-transformed data, was used to compare the equation performance (Armstrong et al., 2001 and references therein). The  $\log(L)$  was calculated as in Moriceau et al. (2009), where a difference in  $\log(L)$  of at least two points is considered as a criterion of a better fit to the observations. The three most recent equations present better RSS, RMSE and  $\log(L)$ , with the new equation presented here providing consistently better statistical results (Table 1).

	Millero et al. (1987)	Santana-Casiano et al. (2005)	Santana- González et al. (2019)	González- Santana et al. (Eq. 4 of this manuscript)
RSS	0.019	0.003	0.006	0.002
RMSE	0.019	0.008	0.011	0.007
$\log(L)$	24.2	33.6	32.5	36.7

Table 1. Statistical comparison of the available Fe(II) oxidation kinetic equations with the measured oxidation rate constants for deep ocean waters without including the hydrothermal neutrally buoyant plumes. Low residual sum of squares (RSS) and root mean square error (RMSE) indicate the best equation fit to observations. Greater than two points of difference in the difference in logarithms of the likelihood ( $\Delta\log(L)$ ) presents a better fit.

### **3.2 Iron(II) oxidation rate constants throughout hydrothermal plumes along the MAR**

Figures 4 and 5 present the half-life times of Fe(II) samples collected above each hydrothermal site with Figure 5 summarizing the results using boxplots. The measured  $t_{1/2}$

values presented a wider range than those determined using the physico-chemical parameters in the improved theoretical equation. The Lost City vent site, was the only station where all the measured  $t_{1/2}$  at  $T_{is}pH_{is}$  conditions presented measured oxidation rate constants higher (shorter  $t_{1/2}$ ) than the theoretically calculated rate constants. At  $T_{25}pH_8$  conditions, all the measured oxidation rate constants were higher than the theoretical ones for all stations except at TAG.

The theoretical  $t_{1/2}$  values presented in Figure 5a, show the expected high variability in the Fe(II) half-life times associated with T, pH and S. These discrepancies were further highlighted in the measured samples, where only Menez Gwen and Lucky Strike theoretical values are within the measured results (a paired t-test did not show a statistical difference between the theoretical and the measured  $t_{1/2}$ , with  $P > 0.35$  for both).

At Menez Gwen (Fig. 4a), measured *in situ*  $t_{1/2}$  varied between 8.3 and 32.0 min ( $k'$  between 0.084 and 0.022  $\text{min}^{-1}$ ), with short measured  $t_{1/2}$  observed in the samples collected at 743, 821, and 827 m. When the temperature was increased and fixed to 25 °C, while the pH was kept at *in situ* conditions (Supplementary Table S1), a significant T effect was observed in  $k'$ , with the measured  $t_{1/2}$  decreasing to less than 4 min. When the pH was fixed to a constant value of 8 along the water column, the measured  $t_{1/2}$  was slightly affected indicating a small effect, as the change in pH was always lower than 0.22. Overall, at  $T_{25}$ , samples presented measured  $t_{1/2}$  in the same order of magnitude as the theoretical  $T_{25}pH_8$ . Samples collected within the lower part of the plume, at less than 30 m above the seafloor (hereafter *asf*) presented higher oxidation rate constants than theoretical ones ( $t_{1/2}$  decreased).

Lucky Strike (Fig. 5a) presented lower oxidation rate constants than Menez Gwen related to lower temperatures in deeper waters (from about 8.5 °C to 4.5 °C). From 1600 m to 1680 m, measured  $t_{1/2}$  averaged  $46.5 \pm 2.5$  min ( $k'$  of  $0.015 \pm 0.001 \text{ min}^{-1}$ ,  $n = 4$ ) (Fig. 4b). This  $t_{1/2}$



344 average is higher than the theoretical value of 39.7 min, while at 1703 m, the Fe(II) half-life  
 345 decreased to 26.3 min ( $k'$  to  $0.026 \text{ min}^{-1}$ ). Overall, at  $T_{25}$ , samples presented measured  $t_{1/2}$  in  
 346 the same order of magnitude as the theoretical  $T_{25} \text{ pH}_8$ . *In situ* pH averaged 7.89, where the  
 347 increase in acidity produced a lower oxidation rate constant than the measured  $t_{1/2}$  at  $T_{25} \text{ pH}_8$ .

348 At Rainbow, station 16, the  $t_{1/2}$  measured at *in situ* conditions presented a wide range of  
 349 variation, from 17.3 to 65.3 min ( $k'$  varied from  $0.040 \text{ min}^{-1}$  to  $0.011 \text{ min}^{-1}$ ). The theoretically  
 350 expected values were within that range, with an average value of  $39 \pm 3 \text{ min}$  ( $n=8$ , Fig. 4c).  
 351 The shortest  $t_{1/2}$  were observed between 1986 m and 2108 m (175 to 295 m *asf*) averaging  
 352  $22.2 \pm 3.6 \text{ min}$  ( $k' = 0.032 \pm 0.006 \text{ min}^{-1}$ ) while the shorter  $t_{1/2}$  were found below the plume  
 353 and above 300 m *asf* (Fig. 4c). The light scattering data shows that the Rainbow plume  
 354 reached heights over 400 m *asf* (although samples were only collected within the first 330 m).  
 355 Temperature was an important factor controlling the oxidation rate constant. At  $T_{25}$   
 356 conditions  $t_{1/2}$  were similar to the theoretical value. When the pH was fixed to 8, small  
 357 changes were observed, and most of the values were close to the theoretical value except for  
 358 those around 1986 m and 2108 m which had shorter  $t_{1/2}$ .

359 Lost City (Fig. 4d), the only alkaline hydrothermal vent, was drastically different from the  
 360 other hydrothermal sites (Fig. 4d), with temperatures around  $10^\circ\text{C}$  and  $\text{pH}_{\text{is}}$  of 8.07  
 361 (Supplementary Table S1). The theoretical  $t_{1/2}$  associated with these temperatures and pH  
 362 ranged between 16 and 20 min. However, most of the measured  $t_{1/2}$  were shorter than 3 min,  
 363 reaching 0.5 min ( $k'$  of  $1.299 \text{ min}^{-1}$ ) at 725 m with the longest  $t_{1/2}$  of 7.8 min ( $k'$  of  $0.088 \text{ min}^{-1}$ )  
 364 at 750 m. At 750 m depth with  $T_{25} \text{ pH}_{\text{is}}$  conditions, the  $t_{1/2}$  decreased to 1.9 min ( $k'$  of  $0.357$   
 365  $\text{min}^{-1}$ ) and further decreased to 1.5 min ( $k'$  of  $0.468 \text{ min}^{-1}$ ) at  $T_{25} \text{ pH}_8$  conditions. All the  
 366 measured  $t_{1/2}$  were significantly shorter than the theoretical  $t_{1/2}$  of 3.2 min ( $k'$  of  $0.218 \text{ min}^{-1}$ )  
 367 at normalized conditions.

Broken Spur presented a wide range in measured  $t_{1/2}$ , with values under *in situ* conditions ranging from 1.0 to 65.1 min ( $k'$  ranging from  $0.714 \text{ min}^{-1}$  at 2929 m to  $0.011 \text{ min}^{-1}$  at 2858 m; Fig. 4e). Two different behaviors can be observed. The two shallowest samples (2820 and 2830 m) were collected in local light scattering minima, with  $t_{1/2}$  averaging  $63.2 \pm 2.7 \text{ min}$  ( $k'$  of  $0.011 \pm 0.001 \text{ min}^{-1}$ ) and values slightly higher than the theoretical ones. Deeper than 2830 m, the samples were collected in local light scattering maxima, where half-life times were shorter with an average  $t_{1/2}$  of  $1.9 \pm 1.2 \text{ min}$  (averaged  $k'$  of  $0.464 \pm 0.220 \text{ min}^{-1}$ ). Experiments at  $T_{25}\text{pH}_8$  also showed that samples below 2830 m presented shorter  $t_{1/2}$  (high  $k'$  values) than what was theoretically expected.

Half-life times measured at *in situ* conditions from the TAG vent site samples presented the widest range in  $t_{1/2}$  (Figs. 4 and 5a), varying from 35.1 to 131.2 min ( $k'$  between  $0.019 \text{ min}^{-1}$  and  $0.005 \text{ min}^{-1}$ ). These samples were characterized by little variability of  $T_{is}$  ( $2.67 \pm 0.01 \text{ }^\circ\text{C}$ ) and  $\text{pH}_{is}$  ( $8.17 \pm 0.01$ ), producing a stable theoretical  $t_{1/2}$  of  $43 \pm 2 \text{ min}$ . Furthermore, the measured  $t_{1/2}$  were the longest obtained in these experiments. When the experiments were repeated at both fixed  $T_{25}$  and  $\text{pH}_8$  the measured values encompassed the theoretical value of 3.3 min, with values slightly higher at around 3325 m (4.3-4.4 min). Therefore, even when temperature and pH affected the observed oxidation rate constants, the high range of values at *in situ* conditions could not be explained by only these two physico-chemical variables.

### **3.3 Investigating the spatial variability of Fe(II) oxidation rate constants around Rainbow and TAG sites**

To investigate the spatial variability in  $t_{1/2}$  for Fe(II), samples were collected from four stations around the Rainbow site at  $0.3^\circ$  (30 km) S (St 15), E (St 12) and W (St 13) and  $1^\circ$  (120 km) E (St 10) (Fig. 1) and from five stations around TAG at  $0.3^\circ$  N (St 26), S (St 27), W (St 30), and E (St 31) and  $1^\circ$  W (St 29) (Fig. 1). At both vent sites, turbidity and light

392 scattering anomalies matched and described the shape of the plume (gray shading in Fig. 4).  
393 The Rainbow plume anomaly was observed between 1930-1995 m, 2060-2090 m, and most  
394 strongly between 2100 and 2210 m. At the TAG site, the signal was three times lower than  
395 that observed at Rainbow, indicating the presence of a lower amount of particles, which could  
396 also be due to a displacement of the sampling with respect to the vent site. The largest  
397 anomalies were measured between 3160-3390 m, with several minor anomalies above (e.g.  
398 2980-3030 m) and below (e.g. 3430-3520 m and 3600-3625 m; Fig. 4).

399 Turbidity and light scattering were useful for tracking the plume displacement even at 30 km  
400 from the vent site. The Rainbow plume was observed to the south and west (Stn. 13 and 15)  
401 at depths between 2000 and 2040 m, and 2270 and 2300 m. For TAG, only stations 27 (south  
402 of TAG, but inside the MAR valley) and 31 (east) showed deeper and thinner turbidity  
403 anomalies between 3400 and 3690 m and a smaller signal between 2920 and 3060 m.

404 For the Rainbow field, samples collected at the vent site in the 1980-2150 m range had  
405 shorter  $t_{1/2}$  at *in situ* conditions (high  $k'$  values) than the theoretical  $t_{1/2}$  (Fig. 6a). All the other  
406 samples (except for Stn 10 at 2430 m) had higher  $t_{1/2}$  values than those calculated  
407 theoretically, and greater  $t_{1/2}$  than observed at Rainbow at depths shallower than 1980 m,  
408 indicating very low oxidation rate constants. This allowed Fe(II) to stay in solution three  
409 times longer than under inorganic seawater conditions. However, when T and pH were fixed  
410 (Fig. 6b), the oxidation rate constants between stations were much closer to the theoretical  
411 value, indicating the T and pH control over the Fe(II) oxidation rate constant. Nevertheless,  
412 plume samples at the 2100-2210 m range and around 2400 m indicated  $t_{1/2}$  values that were  
413 still at least double the theoretical value.

414 At the TAG hydrothermal field, stations situated towards the N and W of TAG presented  
415 shorter  $t_{1/2}$  (high  $k'$  values) than those at the vent site and towards the S and E (Fig. 7a).

Station 30, situated 30 km W of TAG, exhibited both patterns, with long  $t_{1/2}$  (low  $k'$  values) at depths shallower than 2600 m and short  $t_{1/2}$  (high  $k'$  values) at depths below 2700 m. When all the TAG hydrothermal field station samples were normalized (i.e.  $T_{25pH8}$ ; Fig. 7b), most of the variability was removed, and  $t_{1/2}$  averaged  $3 \pm 1.5$  min. The same pattern as for *in situ* conditions was maintained, with stations situated towards the N and W having shorter  $t_{1/2}$  than the theoretical values. These three stations were characterized by their lower turbidity in the deep waters.

### 3.4 The effect of particles, colloids, and organic matter on oxidation rate constants

Experiments with samples from Rainbow (Stn 16, 2051 m), West of Rainbow (Stn 13, 2339 m), Broken Spur (Stn 24, 2829 m) and TAG (Stn 35, 3350 m) were performed to improve our understanding of the impact of particulate and organic matter on the oxidation kinetics of hydrothermal vent fluids. The Rainbow sample at 2051 m, located outside the plume, did not show any difference in the  $\log(k')$  due to the presence of particulates, with values at each pH unit varying by  $\pm 0.03$  and an average slope of  $\log(k')$  against pH of  $0.96 \pm 0.07$  for UF, F0.2 and F0.02 treatments (Fig. 8). For the other three samples (Figs. 8b-d), oxidation rate constants for UF and F0.2 did not present significant differences, with values that were reproducible within  $\pm 0.02$  for the studied pH range. However, F0.02 samples had higher oxidation rate constants, while also maintaining the pH dependence ( $0.95 \pm 0.07$ ). Therefore, the presence of colloidal size particles delayed the oxidation process while not affecting the pH dependence, as shown in Fig. 8, where the intercept changes but the slope is unchanged. All of the UV irradiated samples in Figs. 8a-d indicate that the absence of dissolved organic matter increased the oxidation rate constants. For TAG (3350 m) and Rainbow (2051 m), the  $k'$  values were so high that it was impossible to determine them at pH = 8 under our experimental conditions.

## 4 Discussion

### 4.1. Derived oxidation rate constants as a function of pH and temperature

In the 1990s, Fe(II) oxidation kinetics variability was reported at the TAG hydrothermal field (2-3 min) (Rudnicki and Elderfield, 1993) and near the Juan de Fuca Ridge hydrothermal systems (32 h) (Chin et al., 1994; Massoth et al., 1994) using the Millero et al. (1987) equation. Nevertheless, the variability between those two sites was difficult to explain and reflected fluctuations caused by differences in O<sub>2</sub>, T, and pH among the different sites.

When combining the six hydrothermal vent sites on the MAR (Fig. 9), the relationship between the measured oxidation rate constants under *in situ* conditions against the theoretically derived oxidation rate constants as a function of pH and temperature (in aerated water) can be obtained. Overall, equation 4 can explain 76 out of 104 data points. When color-coding the data points by stations, we observed that all the outliers corresponded to samples that were collected inside hydrothermal plumes (defined by turbidity, light scatter, and redox potential). Consequently, the results obtained from the theoretical equation (Eq. 4) and figure 9, agree well with previous results that O<sub>2</sub>, S, T, and pH can be used to characterize the Fe(II) oxidation rate constant in open ocean waters but not from within hydrothermal plumes.

Our study clearly indicates (Figs. 8 and 9) that the presence of both colloidal particles and dissolved organic matter increases the half-life of Fe(II) (decreased  $k'$ ). This agrees with previous work showing a decrease in the Fe(II) oxidation rate constants in seawater in the presence of some natural organic compounds (Santana-González et al., 2019). However, organic matter can have a positive or negative effect on the oxidation rate constants of Fe(II) depending on the type of organic matter and its degree of remineralization (Rose and Waite,

2003). The variability in the effect of total organic carbon on Fe(II) oxidation proves that total organic carbon cannot be used as a variable in an equation describing  $k'$  (Santana-Casiano et al., 2000; Santana-González et al., 2018; Santana-González et al., 2019). In this sense, a more detailed characterization of organic matter would be necessary, especially in a hydrothermal environment.

#### 4.2. Influence of organic species on Fe(II) oxidation rate constants

The Fe(II) oxidation rate constant (Eq. 5) can be expressed as a function of each Fe(II) species ( $\text{Fe}^{2+}$ ,  $\text{FeOH}^+$ ,  $\text{Fe(OH)}_2$ ,  $\text{FeHCO}_3^+$ ,  $\text{Fe(CO}_3\text{)}$ ,  $\text{Fe(CO}_3\text{)}_2^{2-}$ ,  $\text{Fe(CO}_3\text{)OH}^-$ ,  $\text{FeCl}^+$ ,  $\text{FeSO}_4$ ,  $\text{FeH}_3\text{SiO}_4$  and any organically complexed Fe species). Species such as  $\text{Fe(CO}_3\text{)}_2^{2-}$  and  $\text{Fe(OH)}_2$  could become important at pH higher than 8 (Ussher et al., 2004; González-Davila et al., 2005; Santana-Casiano et al., 2005) in solution. Considering the side reaction coefficient for each inorganic ( $\alpha_i$ ) and organic ( $\alpha_j$ ) Fe(II) species in seawater and the associated second-order oxidation rate constant for the kinetically reactive Fe(II) species ( $k_i$  and  $k_j$ ) (Eq. 6) (Millero and Sotolongo, 1989; King, 1998; Santana-Casiano et al., 2005), the apparent oxidation rate constant can be expressed as:

$$k_{\text{app}} = k_{\text{Fe}^{2+}}\alpha_{\text{Fe}^{2+}} + k_{\text{FeOH}^+}\alpha_{\text{FeOH}^+} + k_{\text{Fe(OH)}_2}\alpha_{\text{Fe(OH)}_2} + k_{\text{FeHCO}_3^+}\alpha_{\text{FeHCO}_3^+} + k_{\text{Fe(CO}_3\text{)}}\alpha_{\text{Fe(CO}_3\text{)}} + k_{\text{Fe(CO}_3\text{)}_2^{2-}}\alpha_{\text{Fe(CO}_3\text{)}_2^{2-}} + k_{\text{Fe(CO}_3\text{)OH}^-}\alpha_{\text{Fe(CO}_3\text{)OH}^-} + k_{\text{FeCl}^+}\alpha_{\text{FeCl}^+} + k_{\text{FeSO}_4}\alpha_{\text{FeSO}_4} + k_{\text{FeH}_3\text{SiO}_4}\alpha_{\text{FeH}_3\text{SiO}_4} + \sum_j k_{\text{FeL}_j}\alpha_{\text{FeL}_j} \quad (5)$$

$$k_{\text{app}} = \sum_i \alpha_i k_i + \sum_j \alpha_j k_j \quad (6)$$

$$\alpha_{\text{Fe}^{2+}} = 1 / \left( 1 + \sum K_{L_i} [L_i] + \sum K_{L_j} [L_j] \right) \quad (7)$$

Where  $\alpha_{\text{Fe}^{2+}}$  is the fraction of free Fe(II) including inorganic and organic speciation,  $[L_i]$  is the concentration of each inorganic ligand with a conditional stability constant  $K_i$  and  $[L_j]$  is

the concentration of each organic ligand with a conditional stability constant  $K_{Lj}$ . The inorganic site reaction coefficient at pH 8 and 25 °C was previously determined as 0.38 (Santana-Casiano et al., 2006). For any inorganic or organic FeL complexes:

$$\alpha_{FeL} = K_{FeL}[L]\alpha_{Fe^{2+}} \quad (8)$$

According to our results, the presence of DOM in solution generated Fe(II)-organic complexes that were overall less reactive to oxidation and therefore, when removed by UV irradiation the resulting oxidation rate constants were higher (Fig. 8).

The amount of dissolved organic carbon (DOC) in the samples ranged between 50 and 79  $\mu\text{mol kg}^{-1}$  (data not shown) and according to O'Sullivan et al. (2005) the maximum amount of  $\text{H}_2\text{O}_2$  produced during irradiation could be 125 to 147  $\text{nmol kg}^{-1}$ , respectively. Following González-Davila et al. (2005) and assuming the extreme case of no  $\text{H}_2\text{O}_2$  decay after 6 days, the UV generated  $\text{H}_2\text{O}_2$  could theoretically increase the Fe(II) oxidation rate constants in oxygen saturated conditions. The theoretical  $t_{1/2}$  associated with the  $\text{H}_2\text{O}_2$  oxidation was between 48 % and 53 % of the  $t_{1/2}$  measured for 0.02  $\mu\text{m}$  filtered samples. Nevertheless, the measured  $t_{1/2}$  for UV-irradiated samples (Supplementary Table S1 and Fig. 8) were shorter (higher  $k'$ ), indicating that any  $\text{H}_2\text{O}_2$  remaining in solution after 6 days was not the main factor that increased the oxidation rate constants and that the presence of dissolved organic matter was stabilizing Fe(II) in solution. Furthermore, laboratory experiments have shown that the  $t_{1/2}$  of  $\text{H}_2\text{O}_2$  in oceanic waters is shorter than 5.5 days (Yuan and Shiller, 2001), therefore the impact of  $\text{H}_2\text{O}_2$  in the experiments would be further reduced.

The role of organically complexed Fe(II) could be calculated from the following assumptions. Firstly, the Fe(II)-L complex was assumed to not oxidize in the pH range of 7.5 to 8. Secondly, the observed reduction in Fe(II) oxidation rate constants (Fig. 8 and

Supplementary Table S1) at 25 °C between the 0.02 µm filtered and the filtered and UV irradiated samples was due to organic complexation. The computed role of organic complexation produced a  $78 \pm 6\%$  decrease in the concentration of reactive inorganic Fe(II) species. The effect of organic Fe(II) species was highest at Broken Spur and TAG sites ( $81 \pm 5\%$ ) and lowest at Rainbow ( $74.1 \pm 4\%$ ). Roy et al. (2008) found a value that was slightly lower for the western subarctic Pacific water, with a  $61 \pm 8\%$  decrease. As both the organic ligand concentrations and the conditional constants are unknown, only the product  $K_{Lj} \cdot [L_j]$  (Eq. 7) can be inferred. Knowing the inorganic distribution coefficient of Fe(II), which is pH dependent but can be calculated from Santana-Casiano et al., (2005), and considering a unique class of ligand (L), the product  $K_{Lj} \cdot [L_j]$  should be  $9 \pm 2$  (higher values at Broken Spur and TAG, while lower values at Rainbow) while  $1 + \sum K_{Li}[L_i]$  in Eq. 7 is 2.6 ( $2.6 = 1/0.38$ , Santana-Casiano et al., (2006)).

If the concentration of Fe(II) organic ligands in seawater is on the same order as Fe(III) ligands (1 to 10 nmol L<sup>-1</sup>), as assumed by Roy et al. (2008), the corresponding conditional constant should range between  $10^9$  to  $10^{10}$ , (respectively for 10 and 1 nmol L<sup>-1</sup> of ligands). The strength of these Fe(II) complexing ligands compared to those for Fe(III) is in the low affinity range (Gledhill and Buck, 2012; Bundy et al., 2014). However, the formation of these complexes would decrease the Fe(II) oxidation rate constant through both the effects on the side reaction coefficients (Eqs. 7-8) and because the complexes can be non-reactive to oxidation or may oxidize slower than other inorganic species. Moreover, it should be considered that organic matter might even increase the Fe(II)  $t_{1/2}$  due to the reduction of organically complexed Fe(III), which would increase the Fe(II) in solution, and therefore the  $t_{1/2}$  (Santana-Casiano et al., 2010).



The UV-irradiation treatment (Fig. 8) removes the organic matter effect on the Fe-complexation, which for the studied samples resulted in an increase in the oxidation rate constants. Consequently, in these analyzed natural samples, organic matter ultimately lowered the oxidation rate constants (black data points below the straight line in Fig. 9).

The DOM is prone to natural and thermal degradation in hydrothermal systems (Hawkes et al., 2016). Accordingly, the variety of organic-complexing ligands and their effect on oxidation could change with plume transport and distance to the vent site as observed in figures 6 and 7. In the proximities to the vent sites, samples presented greater than theoretical oxidation rate constants (above the straight line in Fig. 9). This could be due to the presence of organic matter with ligands complexing Fe that oxidizes faster than the inorganic Fe(II) species. At these locations, the organic ligand effect would dominate over processes that lower oxidation rate constants such as nanoparticle concentrations. Similar experiments considering organic matter degradation just above the vent site should be carried out to confirm this hypothesis. Nevertheless, the complexity of the organic matter pool and the extent and nature of Fe-DOM interactions make the resulting effect on the oxidation rate constants difficult to predict.

#### ***4.3. Effects of physical speciation***

Lough et al. (2019) have shown that there is an Fe exchange between the different particle size fractions within the hydrothermal plume. This exchange could affect Fe(II) oxidation as found in this study for particles smaller than 0.2  $\mu\text{m}$  and colloidal sized particles (0.2-0.02  $\mu\text{m}$ ) at different locations in TAG and in Rainbow (Fig. 8). The results shown in Figure 8 seem to indicate that the size-fractionation can significantly affect Fe(II) oxidation and thus, is a factor that should be considered in future studies. In this sense, previous work has shown that particulate Fe(II), such as pyrite nanoparticles are more resistant to oxidation, with Fe(II)

half-life between 4 and 48 months at 2 °C (Yücel et al., 2011). The presence of colloidal particles also enhances the decay of ROS allowing for longer  $t_{1/2}$  (Yuan and Shiller, 2001). Therefore, nanoparticles could account for a substantial fraction of the decrease in the oxidation rate constants (Fig. 8). Another consequence of filtration is the reduction in larger size organic matter, which could also affect the stabilization of Fe(II) (Buck et al., 2015). The variability observed in the oxidation rate constants inside the plume for the six studied hydrothermal vents indicates that changes in the composition of both the DOM and colloidal particles, both between sites and at different distances from the vent, can strongly affect the oxidation rate constants, thus, their role requires further study.

## 5 Conclusions

This study highlights the complexity of Fe(II) chemistry in the ocean, with a focus on hydrothermal vent settings. Fe(II) oxidation rate constants, and therefore persistence of Fe(II) in the environment, is shown to not only depend on the physico-chemical conditions (T, S, pH, O<sub>2</sub> content) but also the physical state (soluble, colloidal and particulate) of the inorganic and organic species that are present. Our results indicate that organic ligands can stabilize Fe(II) and that nanoparticles present in hydrothermal plumes could increase the resistance to oxidation. Both processes contribute to the observed variability in the oxidation rate constants in the proximities of vents. We were able to revise the theoretical equation for the estimation of  $k'$ , and to further increase the existing temperature range to include seawater temperatures as low as 2 °C. Future studies on iron oxidation kinetics in the marine environment should be accompanied by a characterization of the organic matter present in the medium, a size-fractionation of the samples, and a detailed description of the conventional physico-chemical factors (pH, T, and S).

## Figures

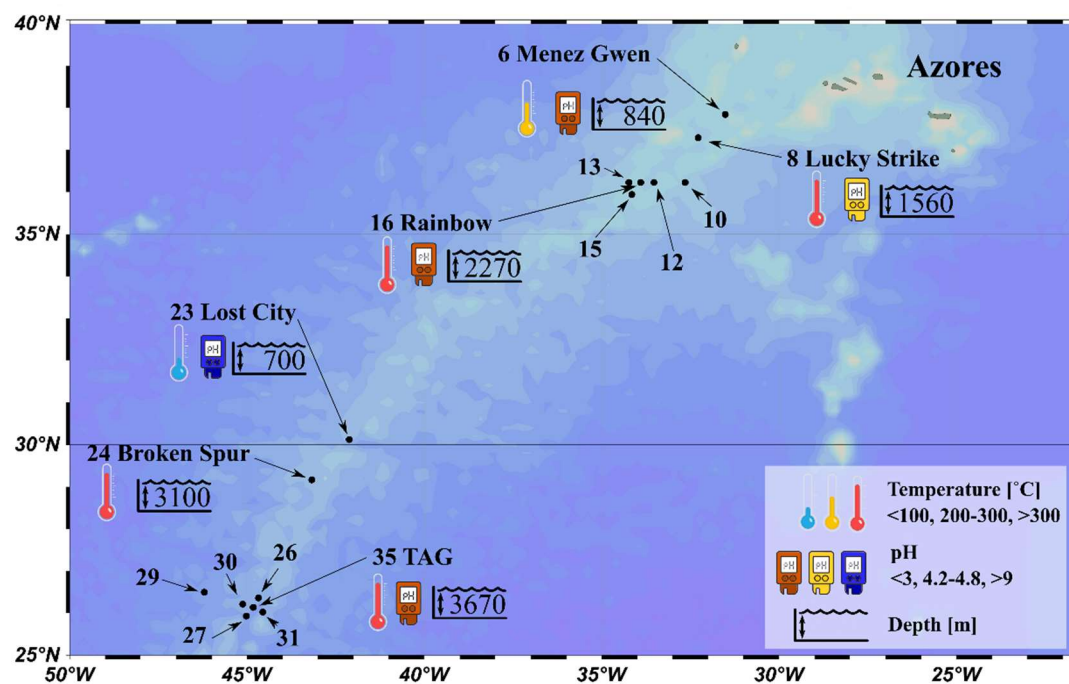
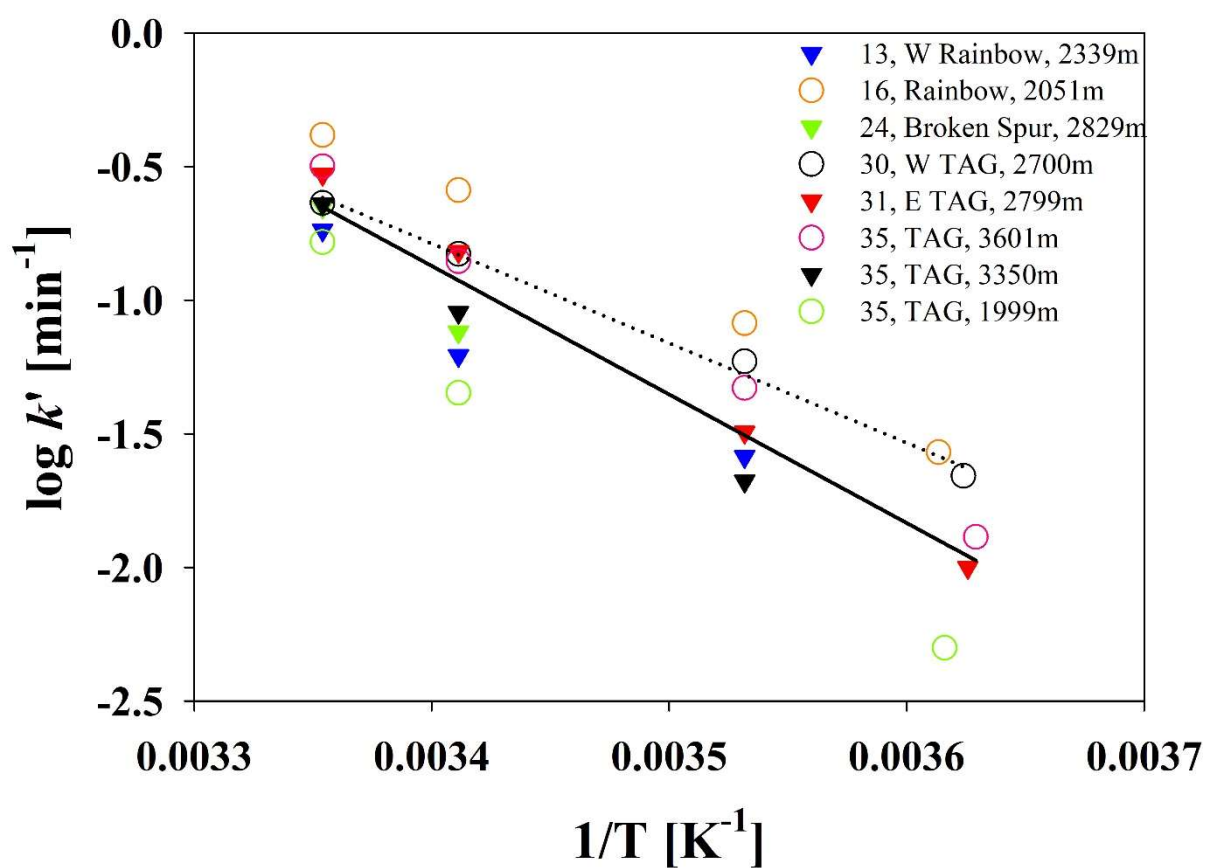
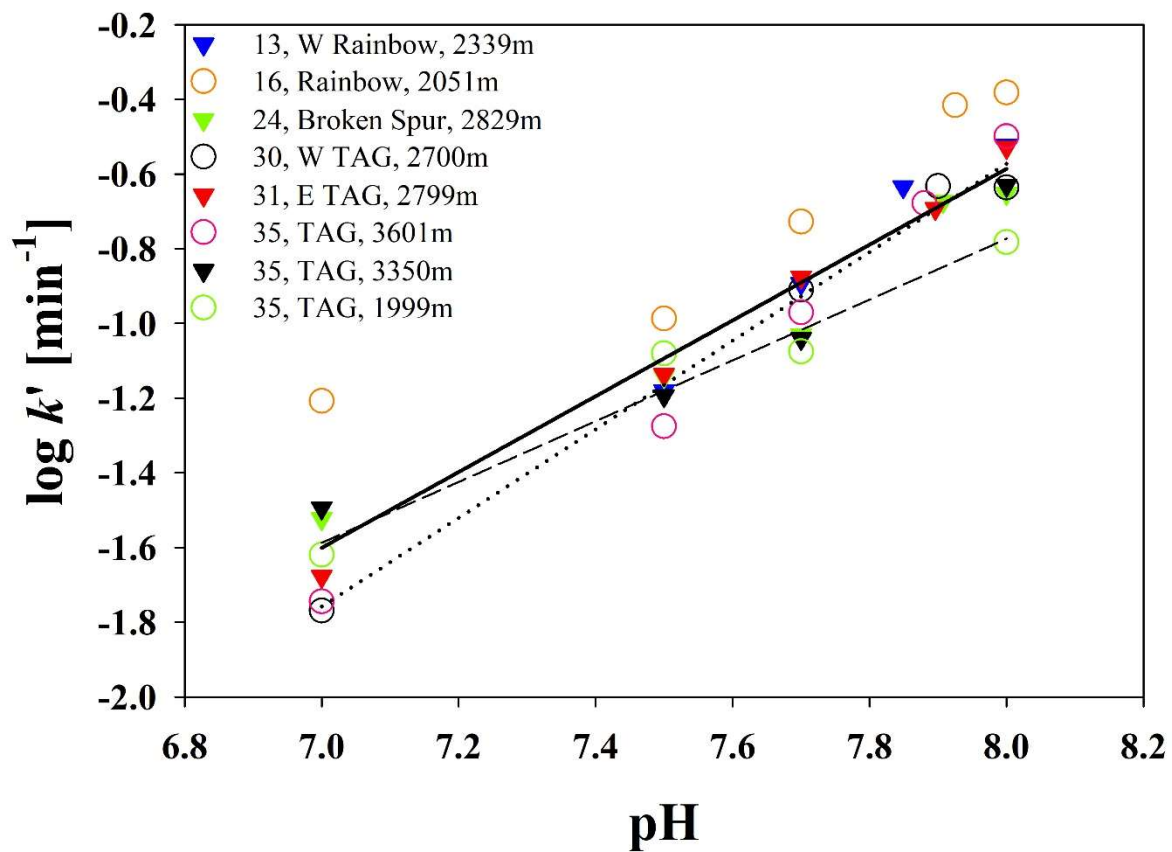


Figure 1. Map of the investigated hydrothermal vent sites along the MAR, showing the station numbers and hydrothermal vent site names for the sampling sites. Symbols represent endmember characteristics. The pH of the Broken Spur endmember was not available.



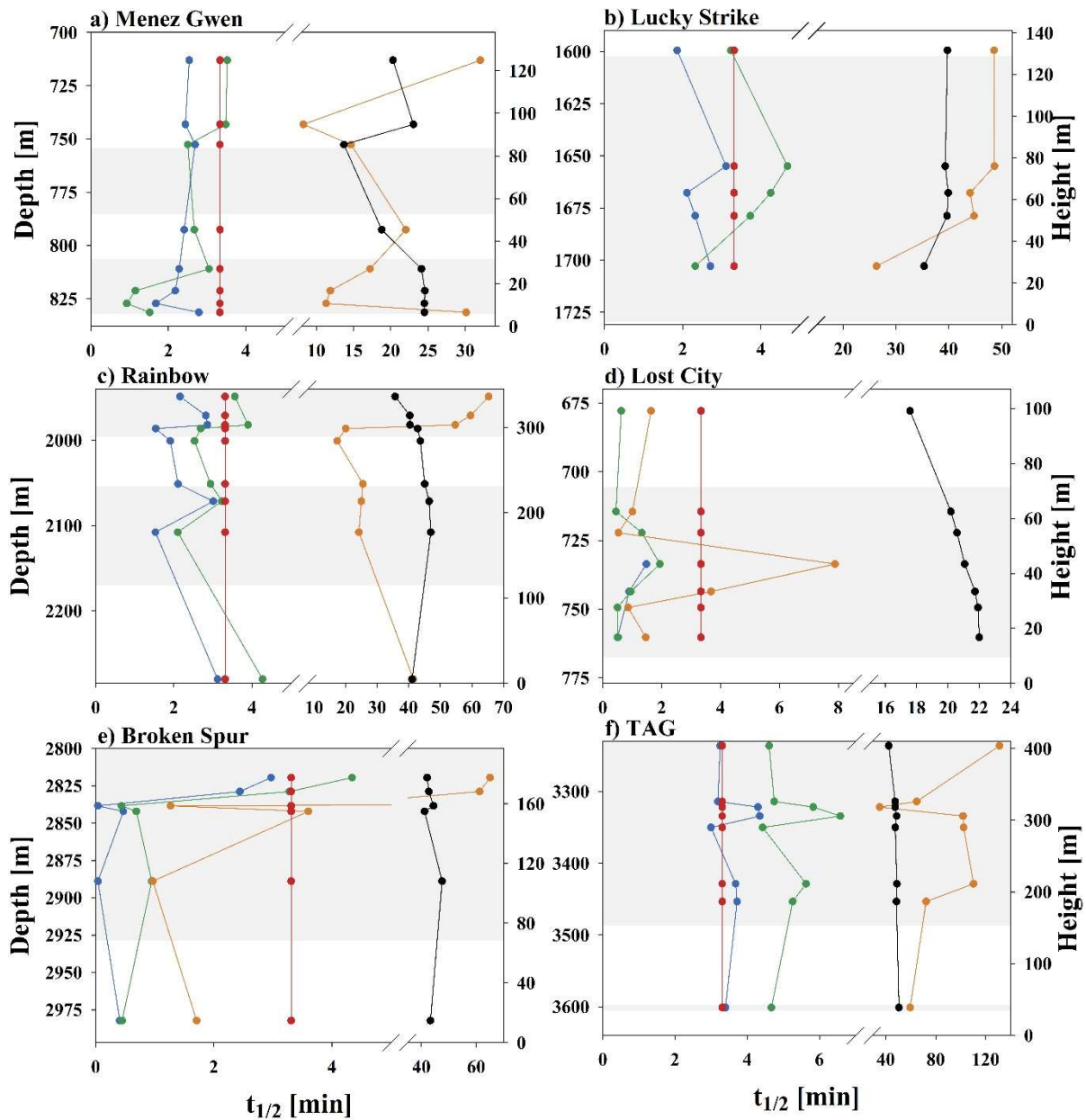
583

Figure 2. Arrhenius relationship between the oxidation rate constant ( $\log k'$  ( $\text{min}^{-1}$ )) and temperature ( $1/T$  ( $\text{K}^{-1}$ )) in the range 2 to 25 °C for eight selected samples. Note that the sample from station 30 (W TAG, 2700m, open squares, dotted line) shows a different behavior than samples from other stations.



588

589 Figure 3. pH effect (from 7.0 to 8.0) on the Fe(II) oxidation rate constants ( $\log k'$  (min<sup>-1</sup>)) for  
 590 eight selected samples collected along the MAR. Note that the samples from 2700 m depth to  
 591 the west of TAG (Stn 30, open squares) and from 1999 m depth at the TAG site (Stn 35, open  
 592 diamonds) have different slopes than samples from other stations (data from these two  
 593 stations are plotted with dotted lines).



594

595 Figure 4. The measured Fe(II) half-life ( $t_{1/2}$ , min) at  $T_{is}pH_{is}$  (orange),  $T_{25}pH_{is}$  (green), and  
596  $T_{25}pH_8$  (blue), and the theoretical (Theo) values for  $T_{is}pH_{is}$  (black), and  $T_{25}pH_8$  (red), at the  
597 six vents. The shaded area shows the anomaly depths determined using light scattering data .  
598 Both, the depth (left y-axis) and the height above the seafloor (right y-axis) of the sampling  
599 are indicated.

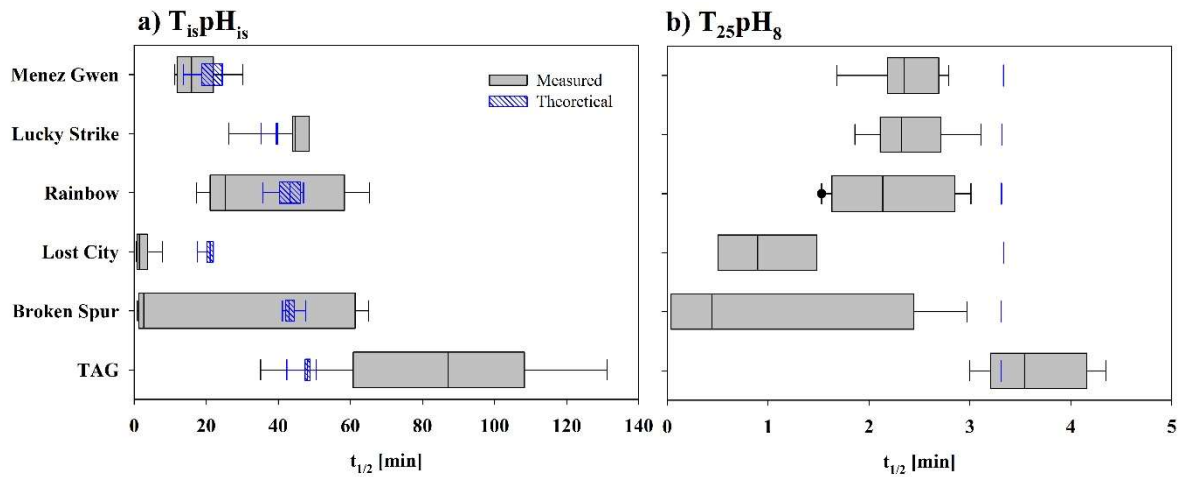


Figure 5. Boxplots of the Fe(II) half-life ( $t_{1/2}$ , min) within the six hydrothermal plumes. a) The measured  $t_{1/2}$  at *in situ* conditions (grey) and the theoretical  $t_{1/2}$  (blue; obtained using Eq. 4). b) The measured  $t_{1/2}$  at constant temperature (25 °C) and pH 8 (grey) and the corresponding theoretical  $t_{1/2}$ , the slight variances are caused by S changes (blue).

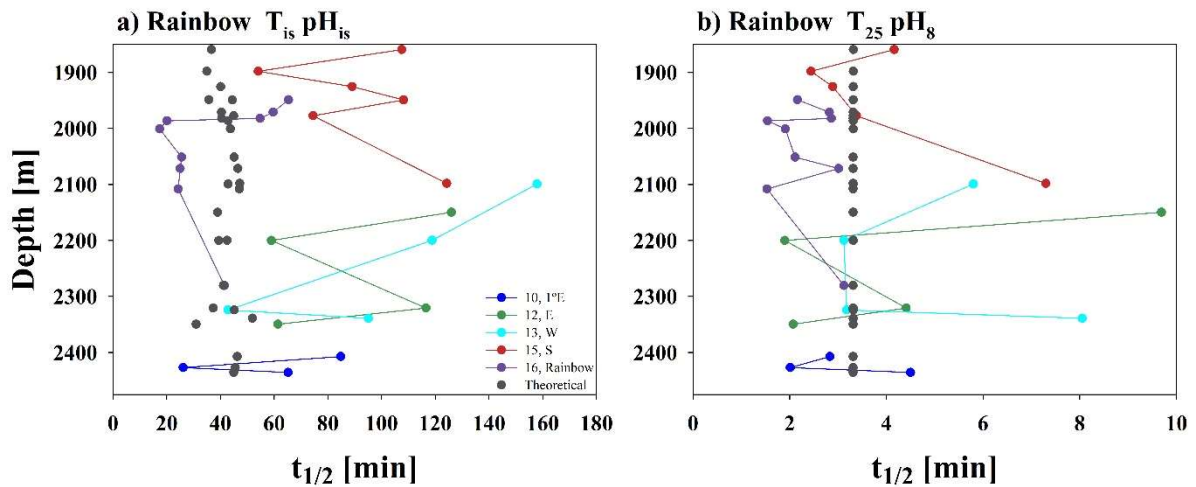


Figure 6. The Fe(II) half-life ( $t_{1/2}$ , min) at the Rainbow field a) under *in situ* conditions (see also Supplementary Table S1) and b) normalized to constant T of 25 °C and a pH of 8.

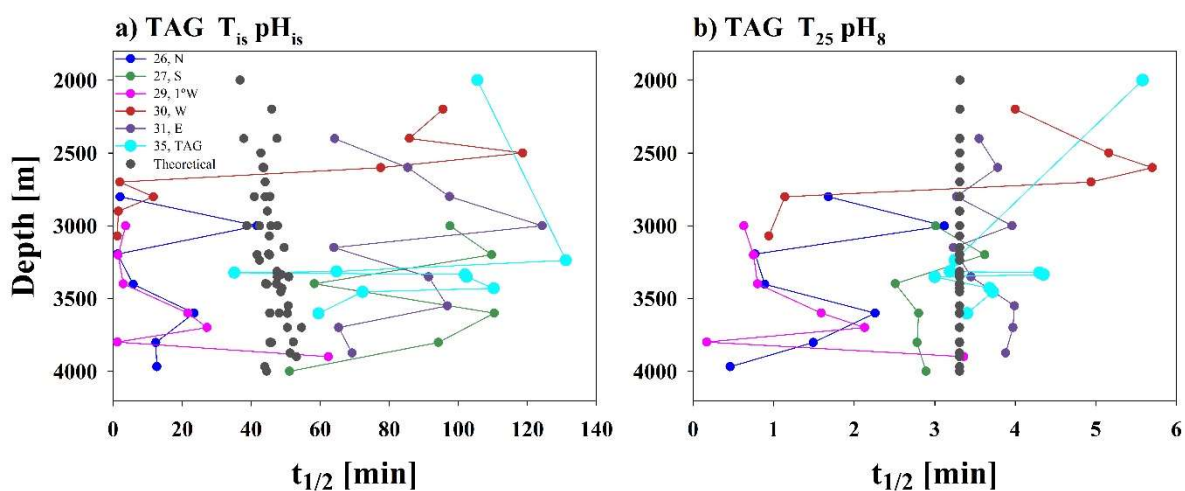


Figure 7. The Fe(II) half-life ( $t_{1/2}$ , min) at the TAG field a) under *in situ* conditions (see also Supplementary Table S1) and b) normalized to constant T of 25 °C and a pH of 8.

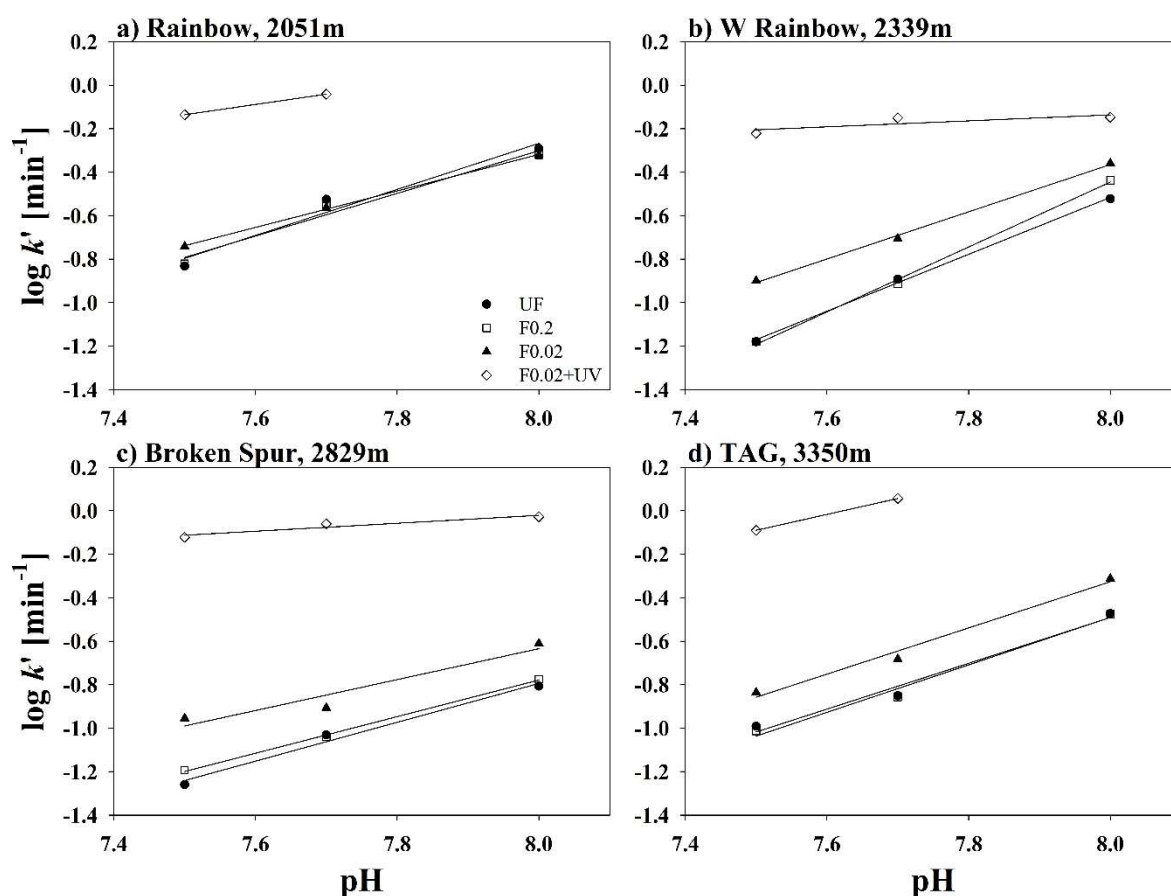
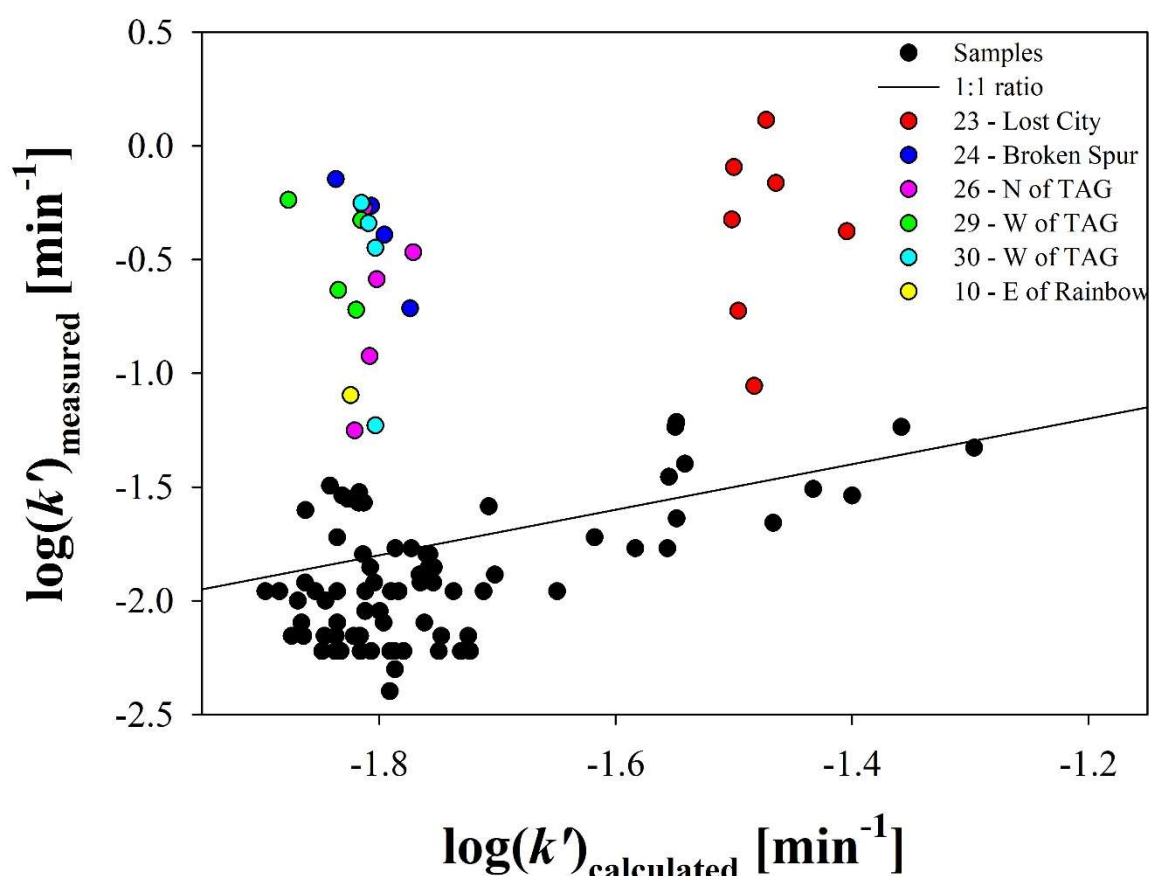


Figure 8. Oxidation rate constants at different pH (7.5, 7.7 and 8), for selected unfiltered (UF, filled circles), filtered through 0.2  $\mu\text{m}$  (F0.2, open squares), filtered through 0.02  $\mu\text{m}$  (F0.02,



614 filled triangles) and filtered through 0.02  $\mu\text{m}$  followed by UV irradiation (F0.02+UV, open  
 615 diamonds) samples at a) Rainbow (Stn 16, 2051 m), b) West of Rainbow (Stn 13, 2339 m), c)  
 616 Broken Spur (Stn 24, 2829 m) and d) TAG (Stn 35, 3350 m).



617  
 618 Figure 9. Fe(II) oxidation rate constants ( $\log(k')$ ) determined under *in situ* conditions against  
 619 the anticipated expected theoretical value. All data points are shown in black. The black line  
 620 represents a 1:1 ratio between both oxidation rate constants. Color coded data points  
 621 correspond to samples with measured oxidation rate constants greater than 20% of the  
 622 theoretically derived rate constants.

623 **Author contributions**

DGS wrote the manuscript with significant contributions from all coauthors. DGS was invited to the research cruise by MCL and AT, where DGS, MCL, and LA collected the samples. DGS analyzed the samples with support from MSC and MGD. Figures for the results were designed by HP and GS. Fieldwork logistics and costs were overseen by MCL and AT, while analysis costs were handled by MSC, MGD, GS, and HP.

## Acknowledgements

The authors would like to thank the captain and crew of the R.R.S. James Cook as well as the scientific team during the GA13 cruise. The field work was supported by NERC (NE/N010396/1 and NE/N009525/1) awards to AT and MCL. This work was supported by ISblue project, Interdisciplinary graduate school for the blue planet (ANR-17-EURE-0015) and co-funded by a grant from the French government under the program "Investissements d'Avenir". Lab work was supported by the ATOPFe CTM2017-83476-P project (Spanish Ministry of Economy and Competitiveness) awarded to MSC and MGD.

## Competing interests

The authors declare no competing interests.

## References

- Andreani M., Escartin J., Delacour A., Ildefonse B., Godard M., Dymont J., Fallick A. E. and Fouquet Y. (2014) Tectonic structure, lithology, and hydrothermal signature of the Rainbow massif (Mid-Atlantic Ridge 36°14'N). *Geochemistry, Geophysics, Geosystems* **15**, 3543–3571.
- Armstrong R. A., Lee C., Hedges J. I., Honjo S. and Wakeham S. G. (2001) A new, mechanistic model for organic carbon fluxes in the ocean based on the quantitative

646 association of POC with ballast minerals. *Deep Sea Res. Part II Top. Stud. Oceanogr.*  
647 **49**, 219–236.

648 de Baar H. J. W. and De Jong J. T. M. (2001) Distributions, sources and sinks of iron in  
649 seawater. In *The Biogeochemistry of Iron in Seawater* (eds. D. Turner and K. A.  
650 Hunter). John Wiley & Sons Ltd., Chichester, UK. pp. 125–253.

651 Bennett S. A., Achterberg E. P., Connelly D. P., Statham P. J., Fones G. R. and German C. R.  
652 (2008) The distribution and stabilisation of dissolved Fe in deep-sea hydrothermal  
653 plumes. *Earth Planet. Sci. Lett.* **270**, 157–167.

654 Buck K. N., Sohst B. and Sedwick P. N. (2015) The organic complexation of dissolved iron  
655 along the U.S. GEOTRACES (GA03) North Atlantic Section. *Deep Sea Res. Part II*  
656 *Top. Stud. Oceanogr.* **116**, 152–165.

657 Bundy R. M., Biller D. V., Buck K. N., Bruland K. W. and Barbeau K. A. (2014) Distinct  
658 pools of dissolved iron-binding ligands in the surface and benthic boundary layer of the  
659 California Current. *Limnol. Oceanogr.* **59**, 769–787.

660 Charlou J. L., Donval J. P., Douville E., Jean-Baptiste P., Radford-Knoery J., Fouquet Y.,  
661 Dapoigny A. and Stievenard M. (2000) Compared geochemical signatures and the  
662 evolution of Menez Gwen (35°50N) and Lucky Strike (37°17N) hydrothermal fluids,  
663 south of the Azores Triple Junction on the Mid-Atlantic Ridge. *Chem. Geol.* **171**, 49–75.

664 Chin C. S., Coale K. H., Elrod V. A., Johnson K. S., Massoth G. J. and Baker E. T. (1994) In  
665 situ observations of dissolved iron and manganese in hydrothermal vent plumes, Juan de  
666 Fuca Ridge. *J. Geophys. Res. Solid Earth* **99**, 4969–4984.

667 Conway T. J. and John S. G. (2014) Quantification of dissolved iron sources to the North

668 Atlantic Ocean. *Nature* **511**, 212–215.

669 Douville E., Charlou J. L., Oelkers E. H., Bienvenu P., Jove Colon C. F., Donval J. P.,  
670 Fouquet Y., Prieur D. and Appriou P. (2002) The rainbow vent fluids (36°14'N, MAR):  
671 The influence of ultramafic rocks and phase separation on trace metal content in Mid-  
672 Atlantic Ridge hydrothermal fluids. *Chem. Geol.* **184**, 37–48.

673 Elderfield H. and Schultz A. (1996) Mid-ocean ridge hydrothermal fluxes and the chemical  
674 composition of the ocean. *Annu. Rev. Earth Planet. Sci.* **24**, 191–224.

675 Field M. P. and Sherrell R. M. (2000) Dissolved and particulate Fe in a hydrothermal plume  
676 at 9°45'N, East Pacific Rise: Slow Fe (II) oxidation kinetics in Pacific plumes. *Geochim.*  
677 *Cosmochim. Acta* **64**, 619–628.

678 Fitzsimmons J. N., John S. G., Marsay C. M., Hoffman C. L., Nicholas S. L., Toner B. M.,  
679 German C. R. and Sherrell R. M. (2017) Iron persistence in a distal hydrothermal plume  
680 supported by dissolved-particulate exchange. *Nat. Geosci.* **10**, 195–201.

681 Fouquet Y., Cambon P., Etoubleau J., Charlou J. L., Ondréas H., Barriga F. J. A. S.,  
682 Cherkashov G., Semkova T., Poroshina I., Bohn M., Donval J. P., Henry K., Murphy P.  
683 and Rouxel O. (2013) Geodiversity of hydrothermal processes along the mid-atlantic  
684 ridge and ultramafic-hosted mineralization: A new type of oceanic Cu-Zn-Co-Au  
685 volcanogenic massive sulfide deposit. *Geophys. Monogr. Ser.* **188**, 321–367.

686 Gamo T., Chiba H., Masuda H., Edmonds H. N., Fujioka K., Kodama Y., Nanba H. and Sano  
687 Y. (1996) Chemical characteristics of hydrothermal fluids from the TAG Mound of the  
688 Mid-Atlantic Ridge in August 1994: Implications for spatial and temporal variability of  
689 hydrothermal activity. *Geophys. Res. Lett.* **23**, 3483–3486.

690 Gartman A. and Findlay A. J. (2020) Impacts of hydrothermal plume processes on oceanic  
691 metal cycles and transport. *Nat. Geosci.* **13**, 396–402.

692 German C. R. and Von Damm K. L. (2004) Hydrothermal processes. In *The Oceans and*  
693 *Marine Geochemistry* (eds. H. D. Holland, K. K. Turekian, and H. Elderfield). Elsevier-  
694 Pergamon. pp. 181–222.

695 Gledhill M. and Buck K. (2012) The Organic Complexation of Iron in the Marine  
696 Environment: A Review. *Front. Microbiol.* **3**, 69.

697 González-Davila M., Santana-Casiano J. M. and Millero F. J. (2005) Oxidation of iron (II)  
698 nanomolar with H<sub>2</sub>O<sub>2</sub> in seawater. *Geochim. Cosmochim. Acta* **69**, 83–93.

699 González-Dávila M., Santana-Casiano J. M. and Millero F. J. (2006) Competition between O<sub>2</sub>  
700 and H<sub>2</sub>O<sub>2</sub> in the oxidation of Fe (II) in natural waters. *J. Solution Chem.* **35**, 95–111.

701 Gray S. E. C., DeGrandpre M. D., Moore T. S., Martz T. R., Friederich G. E. and Johnson K.  
702 S. (2011) Applications of in situ pH measurements for inorganic carbon calculations.  
703 *Mar. Chem.* **125**, 82–90.

704 Hawkes J. A., Hansen C. T., Goldhammer T., Bach W. and Dittmar T. (2016) Molecular  
705 alteration of marine dissolved organic matter under experimental hydrothermal  
706 conditions. *Geochim. Cosmochim. Acta* **175**, 68–85.

707 Hong H. and Kester D. R. (1986) Redox state of iron in the offshore waters of Peru<sup>1</sup>. *Limnol.*  
708 *Oceanogr.* **31**, 512–524.

709 James R. H., Elderfield H. and Palmer M. R. (1995) The chemistry of hydrothermal fluids  
710 from the Broken Spur site, 29 N Mid-Atlantic Ridge. *Geochim. Cosmochim. Acta* **59**,  
711 651–659.

712 Kelley D. S., Karson J. A., Blackman D. K., Früh-Green G. L., Butterfield D. A., Lilley M.  
 713 D., Olson E. J., Schrenk M. O., Roe K. K. and Lebon G. T. (2001) An off-axis  
 714 hydrothermal vent field near the Mid-Atlantic Ridge at 30 N. *Nature* **412**, 145–149.

715 Key R. M., Olsen A., van Heuven S., Lauvset S. K., Velo A., Lin X., Schirnick C., Kozyr A.,  
 716 Tanhua T. and Hoppema M. (2015) Global ocean data analysis project, version 2  
 717 (GLODAPv2).

718 King D. W. (1998) Role of carbonate speciation on the oxidation rate of Fe (II) in aquatic  
 719 systems. *Environ. Sci. Technol.* **32**, 2997–3003.

720 King D. W., Lounsbury H. A. and Millero F. J. (1995) Rates and Mechanism of Fe(II)  
 721 Oxidation at Nanomolar Total Iron Concentrations. *Environ. Sci. Technol.* **29**, 818–824.

722 Lough A. J. M., Homoky W. B., Connelly D. P., Comer-Warner S. A., Nakamura K.,  
 723 Abyaneh M. K., Kaulich B. and Mills R. A. (2019) Soluble iron conservation and  
 724 colloidal iron dynamics in a hydrothermal plume. *Chem. Geol.* **511**, 225–237.

725 Ludwig K. A., Kelley D. S., Butterfield D. A., Nelson B. K. and Früh-Green G. L. (2006)  
 726 Formation and evolution of carbonate chimneys at the Lost City Hydrothermal Field.  
 727 *Geochim. Cosmochim. Acta* **70**, 3625–3645.

728 Lueker T. J., Dickson A. G. and Keeling C. D. (2000) Ocean pCO<sub>2</sub> calculated from dissolved  
 729 inorganic carbon, alkalinity, and equations for K<sub>1</sub> and K<sub>2</sub>: validation based on laboratory  
 730 measurements of CO<sub>2</sub> in gas and seawater at equilibrium. *Mar. Chem.* **70**, 105–119.

731 Mandernack K. W. and Tebo B. M. (1993) Manganese scavenging and oxidation at  
 732 hydrothermal vents and in vent plumes. *Geochim. Cosmochim. Acta* **57**, 3907–3923.

733 Massoth G. J., Baker E. T., Feely R. A., Lupton J. E., Collier R. W., Gendron J. F., Roe K.

- 734 K., Maenner S. M. and Resing J. A. (1998) Manganese and iron in hydrothermal plumes  
735 resulting from the 1996 Gorda Ridge Event. *Deep Sea Res. Part II Top. Stud. Oceanogr.*  
736 **45**, 2683–2712.
- 737 Massoth G. J., Baker E. T., Lupton J. E., Feely R. A., Butterfield D. A., Von Damm K. L.,  
738 Roe K. K. and Lebon G. T. (1994) Temporal and spatial variability of hydrothermal  
739 manganese and iron at Cleft segment, Juan de Fuca Ridge. *J. Geophys. Res. Solid Earth*  
740 **99**, 4905–4923.
- 741 Millero F. J. (1986) The pH of estuarine waters. *Limnol. Oceanogr.* **31**, 839–847.
- 742 Millero F. J. and Sotolongo S. (1989) The oxidation of Fe (II) with H<sub>2</sub>O<sub>2</sub> in seawater.  
743 *Geochim. Cosmochim. Acta* **53**, 1867–1873.
- 744 Millero F. J., Sotolongo S. and Izaguirre M. (1987) The oxidation kinetics of Fe(II) in  
745 seawater. *Geochim. Cosmochim. Acta* **51**, 793–801.
- 746 Millero F. J., Yao W. and Aicher J. (1995) The speciation of Fe (II) and Fe (III) in natural  
747 waters. *Mar. Chem.* **50**, 21–39.
- 748 Moore C. M., Mills M. M., Arrigo K. R., Berman-Frank I., Bopp L., Boyd P. W., Galbraith  
749 E. D., Geider R. J., Guieu C., Jaccard S. L., Jickells T. D., La Roche J., Lenton T. M.,  
750 Mahowald N. M., Marañón E., Marinov I., Moore J. K., Nakatsuka T., Oschlies A.,  
751 Saito M. A., Thingstad T. F., Tsuda A. and Ulloa O. (2013) Processes and patterns of  
752 oceanic nutrient limitation. *Nat. Geosci.* **6**, 701–710.
- 753 Morel F. M. M., Kustka A. B. and Shaked Y. (2008) The role of unchelated Fe in the iron  
754 nutrition of phytoplankton. *Limnol. Oceanogr.* **53**, 400–404.
- 755 Moriceau B., Goutx M., Guigue C., Lee C., Armstrong R., Duflos M., Tamburini C.,

756 Charrière B. and Ragueneau O. (2009) Si–C interactions during degradation of the  
 757 diatom *Skeletonema marinoi*. *Deep Sea Res. Part II Top. Stud. Oceanogr.* **56**, 1381–  
 758 1395.

759 Mottl M. J., Holland H. D. and Corr R. F. (1979) Chemical exchange during hydrothermal  
 760 alteration of basalt by seawater-II. Experimental results for Fe, Mn, and sulfur species.  
 761 *Geochim. Cosmochim. Acta* **43**, 869–884.

762 O’Sullivan D. W., Neale P. J., Coffin R. B., Boyd T. J. and Osburn C. L. (2005)  
 763 Photochemical production of hydrogen peroxide and methylhydroperoxide in coastal  
 764 waters. *Mar. Chem.* **97**, 14–33.

765 Olsen A., Key R. M., Van Heuven S., Lauvset S. K., Velo A., Lin X., Schirnick C., Kozyr A.,  
 766 Tanhua T. and Hoppema M. (2016) The Global Ocean Data Analysis Project version 2  
 767 (GLODAPv2)—an internally consistent data product for the world ocean. *Earth Syst. Sci.*  
 768 *Data* **8**.

769 Resing J. A., Sedwick P. N., German C. R., Jenkins W. J., Moffett J. W., Sohst B. M. and  
 770 Tagliabue A. (2015) Basin-scale transport of hydrothermal dissolved metals across the  
 771 South Pacific Ocean. *Nature* **523**, 200–203.

772 Rose A. L. and Waite T. D. (2003) Effect of dissolved natural organic matter on the kinetics  
 773 of ferrous iron oxygenation in seawater. *Environ. Sci. Technol.* **37**, 4877–4886.

774 Rouxel O., Toner B., Germain Y. and Glazer B. (2018) Geochemical and iron isotopic  
 775 insights into hydrothermal iron oxyhydroxide deposit formation at Loihi Seamount.  
 776 *Geochim. Cosmochim. Acta* **220**, 449–482.

777 Roy E. G. and Wells M. L. (2011) Evidence for regulation of Fe (II) oxidation by organic



778 complexing ligands in the Eastern Subarctic Pacific. *Mar. Chem.* **127**, 115–122.

779 Roy E. G., Wells M. L. and King D. W. (2008) Persistence of iron (II) in surface waters of  
 780 the western subarctic Pacific. *Limnol. Oceanogr.* **53**, 89–98.

781 Rudnicki M. D. and Elderfield H. (1993) A chemical model of the buoyant and neutrally  
 782 buoyant plume above the TAG vent field, 26 degrees N, Mid-Atlantic Ridge. *Geochim.*  
 783 *Cosmochim. Acta* **57**, 2939–2957.

784 Rue E. L. and Bruland K. W. (1995) Complexation of iron(III) by natural organic ligands in  
 785 the Central North Pacific as determined by a new competitive ligand  
 786 equilibration/adsorptive cathodic stripping voltammetric method. *Mar. Chem.* **50**, 117–  
 787 138.

788 Santana-Casiano J. M., González-Dávila M., González A. G. and Millero F. J. (2010) Fe (III)  
 789 reduction in the presence of catechol in seawater. *Aquat. geochemistry* **16**, 467–482.

790 Santana-Casiano J. M., González-Dávila M. and Millero F. J. (2005) Oxidation of nanomolar  
 791 level of Fe(II) with oxygen in natural waters. *Environ. Sci. Technol.* **39**, 2073–2079.

792 Santana-Casiano J. M., González-Dávila M. and Millero F. J. (2006) The role of Fe(II)  
 793 species on the oxidation of Fe(II) in natural waters in the presence of O<sub>2</sub> and H<sub>2</sub>O<sub>2</sub>. *Mar.*  
 794 *Chem.* **99**, 70–82.

795 Santana-Casiano J. M., González-Dávila M., Rodríguez M. J. and Millero F. J. (2000) The  
 796 effect of organic compounds in the oxidation kinetics of Fe(II). *Mar. Chem.* **70**, 211–  
 797 222.

798 Santana-González C., González-Dávila M., Santana-Casiano J. M., Gladyshev S. and Sokov  
 799 A. (2019) Organic matter effect on Fe (II) oxidation kinetics in the Labrador Sea. *Chem.*

800        *Geol.* **511**, 238–255.

801    Santana-González C., Santana-Casiano J. M., González-Dávila M. and Fraile-Nuez E. (2017)

802        Emissions of Fe(II) and its kinetic of oxidation at Tagoro submarine volcano, El Hierro.

803        *Mar. Chem.* **195**, 129–137.

804    Santana-González C., Santana-Casiano J. M., González-Dávila M., Santana-del Pino A.,

805        Gladyshev S. and Sokov A. (2018) Fe (II) oxidation kinetics in the North Atlantic along

806        the 59.5° N during 2016. *Mar. Chem.* **203**, 64–77.

807    Searle R. (2013) *Mid-ocean ridges.*, Cambridge University Press.

808    Shaked Y., Kustka A. B. and Morel F. M. M. (2005) A general kinetic model for iron

809        acquisition by eukaryotic phytoplankton. *Limnol. Oceanogr.* **50**, 872–882.

810    Statham P. J., German C. R. and Connelly D. P. (2005) Iron (II) distribution and oxidation

811        kinetics in hydrothermal plumes at the Kairei and Edmond vent sites, Indian Ocean.

812        *Earth Planet. Sci. Lett.* **236**, 588–596.

813    Stumm W. and Lee G. F. (1961) Oxygenation of ferrous iron. *Ind. Eng. Chem.* **53**, 143–146.

814    Tagliabue A., Bopp L., Dutay J. C., Bowie A. R., Chever F., Jean-Baptiste P., Bucciarelli E.,

815        Lannuzel D., Remenyi T., Sarthou G., Aumont O., Gehlen M. and Jeandel C. (2010)

816        Hydrothermal contribution to the oceanic dissolved iron inventory. *Nat. Geosci.* **3**, 252–

817        256.

818    Tagliabue A., Bowie A. R., Boyd P. W., Buck K. N., Johnson K. S. and Saito M. A. (2017)

819        The integral role of iron in ocean biogeochemistry. *Nature* **543**, 51–59.

820    Tagliabue A. and Völker C. (2011) Towards accounting for dissolved iron speciation in

821 global ocean models. *Biogeosciences* **8**, 3025–3039.

822 Ussher S. J., Achterberg E. P. and Worsfold P. J. (2004) Marine biogeochemistry of iron.

823 *Environ. Chem.* **1**, 67–80.

824 Voelker B. M. and Sedlak D. L. (1995) Iron reduction by photoproduced superoxide in

825 seawater. *Mar. Chem.* **50**, 93–102.

826 Voelker B. M. and Sulzberger B. (1996) Effects of fulvic acid on Fe (II) oxidation by

827 hydrogen peroxide. *Environ. Sci. Technol.* **30**, 1106–1114.

828 Wang H., Yang Q., Ji F., Lilley M. D. and Zhou H. (2012) The geochemical characteristics

829 and Fe (II) oxidation kinetics of hydrothermal plumes at the Southwest Indian Ridge.

830 *Mar. Chem.* **134**, 29–35.

831 Yuan J. and Shiller A. M. (2001) The distribution of hydrogen peroxide in the southern and

832 central Atlantic ocean. *Deep Sea Res. Part II Top. Stud. Oceanogr.* **48**, 2947–2970.

833 Yücel M., Gartman A., Chan C. S. and Luther G. W. (2011) *Hydrothermal vents as a*

834 *kinetically stable source of iron-sulphide-bearing nanoparticles to the ocean.*, Nature

835 Publishing Group.

836